

Discrete-element modeling of nacre-like materials: Effects of random microstructures on strain localization and mechanical performance



Najmul Abid, Mohammad Mirkhalaf, Francois Barthelat*

Department of Mechanical Engineering, McGill University, 817 Sherbrooke Street West, Montreal, QC H3A 2K6, Canada

ARTICLE INFO

Article history:

Received 23 June 2017

Revised 12 September 2017

Accepted 7 November 2017

Available online 7 December 2017

Keywords:

Discrete element modeling

Staggered composites

Biological and bio-inspired materials

Nacre

Bone

ABSTRACT

Natural materials such as nacre, collagen, and spider silk are composed of staggered stiff and strong inclusions in a softer matrix. This type of hybrid microstructure results in remarkable combinations of stiffness, strength, and toughness and it now inspires novel classes of high-performance composites. However, the analytical and numerical approaches used to predict and optimize the mechanics of staggered composites often neglect statistical variations and inhomogeneities, which may have significant impacts on modulus, strength, and toughness. Here we present an analysis of localization using small representative volume elements (RVEs) and large scale statistical volume elements (SVEs) based on the discrete element method (DEM). DEM is an efficient numerical method which enabled the evaluation of more than 10,000 microstructures in this study, each including about 5,000 inclusions. The models explore the combined effects of statistics, inclusion arrangement, and interface properties. We find that statistical variations have a negative effect on all properties, in particular on the ductility and energy absorption because randomness precipitates the localization of deformations. However, the results also show that the negative effects of random microstructures can be offset by interfaces with large strain at failure accompanied by strain hardening. More specifically, this quantitative study reveals an optimal range of interface properties where the interfaces are the most effective at delaying localization. These findings show how carefully designed interfaces in bioinspired staggered composites can offset the negative effects of microstructural randomness, which is inherent to most current fabrication methods.

© 2017 Elsevier Ltd. All rights reserved.

1. Introduction

The outstanding mechanical properties of mineralized biological materials such as bone (Ritchie et al., 2009; Jäger and Fratzl, 2000) or mollusk shells (Barthelat et al., 2007) result from complex interactions between their soft and hard phases. A prominent microstructure in these materials is the *staggered* arrangement in which elongated mineral inclusions are aligned with the direction of loading in a “brick and mortar” fashion where the mortar consists of soft bio-polymeric layers (Weiner and Addadi, 1997). For example, nacre found in the inner layer of sea shells is composed of ~95 wt% microscopic aragonite tablets which are arranged in a staggered structure and joined by ~5 wt% bio-polymers interfaces (Fig. 1a) (Jackson et al., 1988). Another example of staggered structures is bone (Fig. 1b). At the millimeter scale, cortical bone is

* Corresponding author

E-mail address: francois.barthelat@mcgill.ca (F. Barthelat).

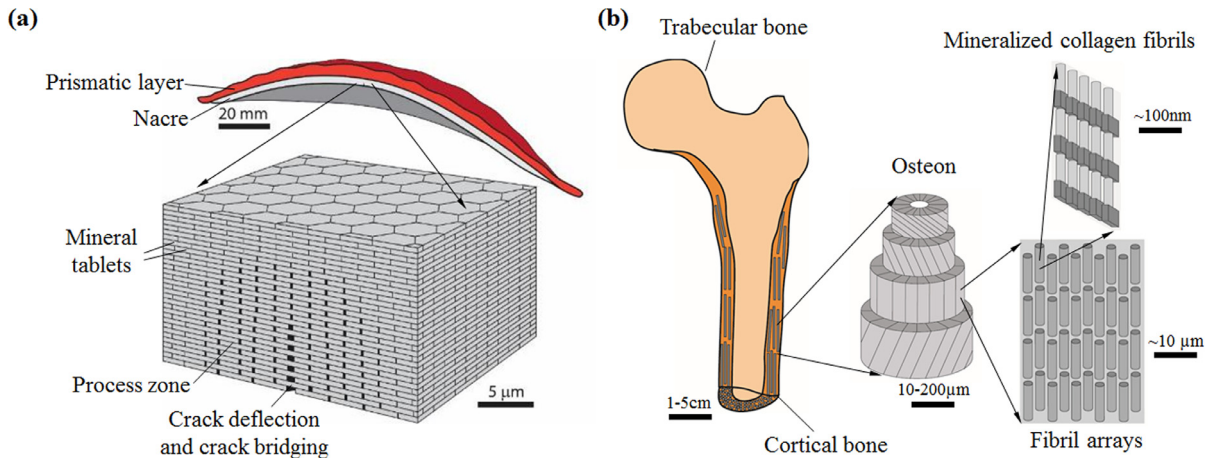


Fig. 1. Two examples of staggered structures in highly mineralized biological materials. (a) Nacre found in the inner layer of sea shells is composed of a stagger of micron-sized aragonite tablets, (b) Cortical bone, at the nanoscale, is composed of mineralized collagen fibrils which are arranged in a staggered structure.

composed of osteons, which are separated by weaker interfaces (cement lines). Osteons themselves are made of concentric layers of unidirectional collagen fibers with varying fiber direction in the neighboring layers. Each fiber consists of a staggered arrangement of fibrils, with each fibril being a staggered assembly of tropocollagen molecules and elongated nano-minerals (Fig. 1b). Similar staggered architectures are found in silk drag line produced by spiders, where beta sheet nanocrystals of proteins are embedded in an amorphous proteinaceous matrix, with the nanocrystals aligned with the tensile direction (Keten et al., 2010). The staggered structure, therefore, appears to be pervasive in load bearing biological materials (Wegst and Ashby, 2004), and it is found in plant or animal species with no common evolutionary descent. Interestingly, recent theoretical investigations show that the staggered architecture indeed provides an optimum combination of stiffness, strength, and toughness (Guo and Gao, 2006; Rabiei et al., 2010; Begley et al., 2012; Barthelat and Mirkhalaf, 2013; Barthelat, 2014), suggesting that this architecture is the result of an interesting case of parallel evolution. The remarkable combinations of properties generated by natural staggered architectures have motivated the development of bio-inspired composites fabricated with using self-assembly (Bonderer et al., 2008; Valashani et al., 2015), freeze casting (Deville et al., 2006), filtration (Liu et al., 2011), sedimentation (Behr et al., 2015), doctor blading (Mirkhalaf and Barthelat, 2016) or controlled mineralization (Mao et al., 2016). These methods produce “nacre-like” microstructures, but the statistical variation and randomness in these microstructures is significant and much larger than what is found in natural nacre or bone. Perfectly periodic staggered arrangements can be fabricated by only at larger length scales in “architected materials” and using manual assembly (Barthelat and Zhu, 2011), 3D printing (Espinosa et al., 2011) or laser engraving (Chintapalli et al., 2014; Valashani and Barthelat, 2015).

The mechanical properties of staggered composites are governed by the hard inclusions gliding over one another, a specific mechanism which is mediated by the shearing of the softer interfaces. This mechanism generates nonlinear deformations and powerful toughening mechanisms that include crack deflection, bridging, wide inelastic process zone (Fig. 1a) (Jäger and Fratzl, 2000; Barthelat and Rabiei, 2011; Barthelat et al., 2016). Several analytical and numerical models have been developed in the past to predict the stiffness, strength, and toughness of staggered composites as a function of microstructure and of the properties of the hard and soft phases. Many of these models are based on a small, two-dimensional representative volume elements (RVEs) which consists of two or four tablets and which are used to predict and optimize modulus, strength or energy absorption as function of microstructure and properties of the base components (Jäger and Fratzl, 2000; Jackson et al., 1988; Begley et al., 2012; Barthelat, 2014; Kotha et al., 2001; Bar-On and Wagner, 2011; Gao, 2006). The RVE approach assumes that (i) the material is perfectly periodic, (ii) all the tablets and interfaces fail and deform simultaneously and identically within the material, so that nonlinear deformations are assumed to propagate uniformly over large volumes with no strain localization. In reality, biological and bioinspired staggered materials display pronounced microstructural variations and composition heterogeneity, which can have profound impact on material performance (Alava et al., 2006; Dimas et al., 2014). For example, models based on weakest link theory (Zhang et al., 2010) and Monte Carlo simulations (Wei et al., 2015) have shown a reduction of strength from statistical variation in tablet overlaps. Introducing a single defect in a chain of otherwise perfect shear-lap models can precipitate localization and failure (Chintapalli et al., 2014). Designing and optimizing bio-inspired composites based on simple RVE modeling may therefore lead to poorly performing actual materials if variations in microstructure are not taken into account at the modeling stage. Numerical models that included a large number of tablets were more recently proposed to capture structure-property relationships on larger volumes (Barthelat et al., 2007; Katti and Katti, 2001; Askarinejad and Rahbar, 2015; Pro et al., 2015). While each of these models could capture effects that small RVEs could not, they also have their own limitations: some of them only consider elastic

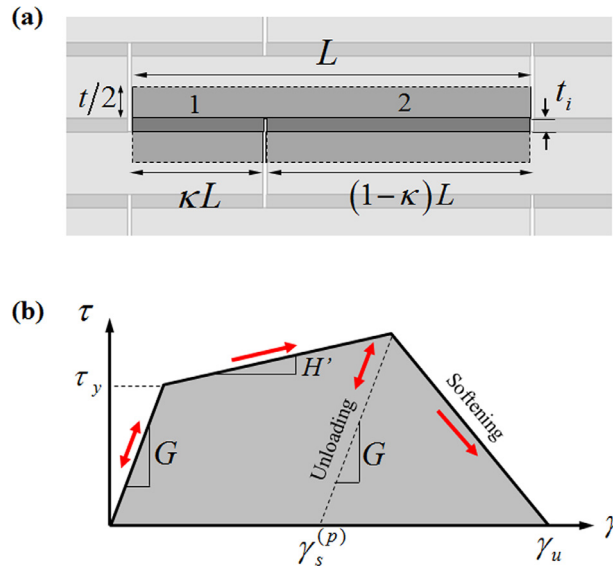


Fig. 2. (a) Single cell RVE with key dimensions; (b) shear stress-strain curve showing the five independent parameters G , τ_y , H , $\gamma_s^{(p)}$ and γ_u .

response and brittle failure (Katti and Katti, 2001; Askarinejad and Rahbar, 2015), or used simplified flow rules at the interfaces (Pro et al., 2015). Some of the most accurate models for this material (Barthelat et al., 2007; Mirkhalaf and Barthelat, 2016; Katti and Katti, 2001; Niebel et al., 2016; Anup, 2015) use finite elements, which is computationally expensive. Only a limited number of tablets can be included, and therefore they cannot capture microstructural variations and become “statistical volume elements” (Ostoj-Starzewski, 2006; Ostoj-Starzewski et al., 2007). Moreover, these models cannot be used to explore the large number of statistical realizations which is needed to accurately capture the effects of statistical variations on mechanical performance (Yin et al., 2008). Discrete element models have also been used for staggered composites (Pro et al., 2015; Chandler and Cheng, 2017; Pro et al., 2015; Lim et al., 2016). This method offers significant savings in terms of computational cost, but it is relatively recent and has not been widely used for this type of material so far. Most of these studies conclude that statistical variations in microstructures degrade overall mechanical properties. However, there are also identified configurations where statistics is beneficial. In ductile crack growth, for example, non-uniform distributions of obstacles produce tougher materials than when the obstacles are equally spaced (Needleman and Tvergaard, 1991). Large 3D finite elements models of nacre have suggested that some random variations in the microstructure can help strength and strain hardening (Barthelat et al., 2007). The exact effect of statistical microstructure on mechanical performance, in particular the ductility and toughness, therefore remains an open question for staggered composites. The implications are important in the design of bio-inspired materials.

The present study focuses on the effect of statistical variations of microstructure on the mechanical performance of staggered composites, focusing on strain localization and strain at failure. We first use a small RVE to capture the effects of defect and localization in the simplest way possible. We then present large scale discrete element models of staggered composites where we parameterize the amount of statistical variation in the microstructure, the properties of the interfaces, and the type of arrangement for the inclusions.

2. Two-interface, small representative volume element (RVE)

We first capture the mechanism of localization with a small RVE or in other words a unit cell (Fig. 2a). This RVE represents a perfectly periodic staggered composite composed of tablets of length L and thickness t , that are bonded together by an interface of thickness t_i . The tablets partially overlap, defining a “short” overlap region of length κL (labeled 1 on Fig. 2a) and “long” overlap region of length $(1-\kappa)L$ (labeled 2 on Fig. 2a). We do not take any size effect into account here so that the microstructure is captured by three independent parameters: the non-dimensional tablet aspect ratio $\rho = \frac{L}{t}$, the overlap ratio κ ($0 < \kappa \leq 0.5$, where $\kappa = 0.5$ corresponds to what we now refer to as “perfect microstructure”), and tablet volume concentration $\phi = \frac{t}{t+t_i}$ ($0 < \phi < 1$). Considering symmetries, only half of the thickness of the tablets is modeled in the RVE. This type of model, based on classical shear lag theory (Tsai et al., 1998; Volkersen, 1938), has been used extensively in the past, with an “asymmetry” in the overlap of the tablets (Yourdkhani et al., 2011). However, here we present a new interpretation where the asymmetry of overlaps acts as a measure of imperfections in the microstructure, because the shorter overlap is weaker than the longer one. By this measure, a “perfect” microstructure has tablets overlapping by exactly one half of their length ($\kappa = 0.5$), while in the “imperfect” microstructures one or more of the overlaps may be longer than the other ($\kappa < 0.5$).

In this model, the response of the interfaces in shear is governed by the stress-strain curve shown on Fig. 2b. An initial linear elastic region with shear modulus G is followed by yielding at $\tau = \tau_y$, and by a post yield region with strain hardening: $\tau = \tau_y + H\gamma^{(p)}$. Here, H is the hardening slope and $\gamma^{(p)}$ is the plastic strain at the interface with $\gamma^{(p)} = \gamma - \frac{\tau}{G}$ (as a result, the slope of the stress-strain curve in the yielding region is $H' = H/(1 + H/G)$). A final linear softening segment starts at $\gamma^{(p)} = \gamma_s^{(p)}$ until the ultimate shear strain γ_u at which the stress vanishes. Therefore, this shear stress-strain curve is defined by five independent parameters: G , τ_y , H , $\gamma_s^{(p)}$, and γ_u . We chose this three-step cohesive law because it is typical of deformable engineering adhesives (Chalkley and Chiu, 1993) and bio-polymers (Smith et al., 1999). For convenience, we use the terms such as “yield point”, “hardening” or “ductile” which are typically associated with the mechanics of metals, even-though the materials in natural or bio-inspired composites may not be metallic. The cohesive traction-separation law for the interface can be obtained by computing the displacement jump $\Delta u = t_i \gamma$ across the interfaces as a function of shear strain. In terms of micromechanics, the mechanical properties of the staggered composites are governed by the way the elongated inclusions channel and amplify the shear response of the interfaces. Since the inclusions (or “bricks”) in biological and bioinspired materials are several orders of magnitude stiffer than the interfaces, we modeled them as rigid in this study. The assumption of rigid tablets has three important implications: (i) deformations are only generated by the interfaces between the tablets; (ii) the shear stress at the interfaces is uniform; (iii) there is no peeling stress at the interfaces, so the interface is only loaded in shear. Using load transfer and continuity equations, an analytical solution can be derived for the RVE in tension. The transfer of stress from shear at the interface to tension in the tablets is written:

$$\sigma = \phi \kappa \rho \tau_1 \quad (1)$$

Where τ_1 is the shear stress carried by interface 1. For continuity of stress:

$$\kappa \tau_1 = (1 - \kappa) \tau_2 \quad (2)$$

where τ_1 is the shear stress carried by interface 2. Note that here $\tau_1 \geq \tau_2$ since we chose $0 < \kappa \leq 0.5$. Differentiating the equation leads to:

$$\kappa \frac{d\tau_1}{d\gamma_1} = (1 - \kappa) \frac{d\tau_2}{d\gamma_2} \frac{d\gamma_2}{d\gamma_1} \text{ or } \frac{d\gamma_2}{d\gamma_1} = \frac{\kappa}{1 - \kappa} \frac{\alpha_1}{\alpha_2} \text{ with } \begin{cases} \alpha_1 = \frac{1}{G} \frac{d\tau_1}{d\gamma_1} \\ \alpha_2 = \frac{1}{G} \frac{d\tau_2}{d\gamma_2} \end{cases} \quad (3)$$

The tensile strain in the RVE is:

$$\bar{\varepsilon} = \frac{\Delta u_1 + \Delta u_2}{L} = \frac{1}{\rho} \frac{1 - \phi}{\phi} (\gamma_1 + \gamma_2) \quad (4)$$

Differentiating (1) and (4) gives:

$$d\sigma = \phi \kappa \rho d\tau_1 \quad (5)$$

$$d\varepsilon = \frac{1}{\rho} \frac{1 - \phi}{\phi} (d\gamma_1 + d\gamma_2) \quad (6)$$

Combining these two equations provides:

$$\frac{d\sigma}{d\varepsilon} = \frac{\phi^2}{1 - \phi} \frac{\rho^2}{\left(\frac{1}{\kappa\alpha_1} + \frac{1}{(1-\kappa)\alpha_2}\right)} G \quad (7)$$

This expression provides the slope of the stress-strain curve as a function of the behavior of the interfaces and the microstructure. Because the cohesive law is a piecewise linear function, we expect the tensile stress-strain curve of the RVE to also be a piecewise linear function. Using Eq. (7), we can now compute the slope of each segment of the tensile stress-strain curve from the cohesive law. Table 1 gives the slope of the stress-strain curve in different regimes for interfaces 1 and 2.

The first regime corresponds to linear elastic deformations in interfaces 1 and 2, and the model provides the tensile modulus E of the RVE. In the second regime “post-yield mode 1” the weaker interface 1 yields, but interface 2 remains elastic. The modulus and first yield strength of the RVE can be normalized by the modulus and yield strength of a “perfect” microstructure with $\kappa = 0.5$. This gives:

$$E/E_0 = 4\kappa(1 - \kappa) \quad (8)$$

$$\sigma_y/\sigma_0 = 2\kappa \quad (9)$$

These relations, displayed on Fig. 4a and b, are typical for this type of material. Here we focus on post yield regimes and strain at softening. Post yield mode (1) ends either by premature softening if $\gamma_1 = \gamma_s$ (softening mode (1), Fig. 3a), or with a second yield point when interface 2 yields at $\tau_2 = \tau_y$ (post yield mode (2)). Post yield mode (2) is followed by softening

Table 1

Slope of the tensile stress strain curve at different regimes of tensile deformation for the RVE, computed using Eq. (7).

Regime	α_1	α_2	Slope on tensile stress-strain curve
Linear elastic	1	1	$\frac{d\sigma}{d\varepsilon} = E = \frac{\phi^2}{1-\phi} \kappa (1-\kappa) \rho^2 G$
Post-yield mode (1): Interface 1 yields, Interface 2 elastic	$\frac{1}{G/H+1}$	1	$\frac{d\sigma}{d\varepsilon} = \frac{\phi^2}{1-\phi} \frac{\kappa \rho^2}{(G/H+1/(1-\kappa))} G$
Post-yield mode (2): Interfaces 1 and 2 yield (condition: Eq. (10))	$\frac{1}{G/H+1}$	$\frac{1}{G/H+1}$	$\frac{d\sigma}{d\varepsilon} = \frac{\phi^2}{1-\phi} \frac{\rho^2 \kappa (1-\kappa)}{G/H+1} G$
Softening mode (1): Interface 1 softens from post-yield mode (1), interface 2 unloads from elastic regime	$\frac{\frac{G}{\tau_y} [\gamma_s^{(p)} - \gamma_u] + 1}{1}$	1	$\frac{d\sigma}{d\varepsilon} = \frac{\phi^2}{1-\phi} \frac{\rho^2 \kappa (1-\kappa)}{\frac{G}{\tau_y} (1-\kappa) (\gamma_s^{(p)} - \gamma_u) + 1} G$
Softening mode (2): Interface 1 softens from post-yield mode (2), interface 2 unloads from yielding	$\frac{1}{\frac{G}{\tau_y} [\gamma_s^{(p)} - \gamma_u] + 1}$	1	$\frac{d\sigma}{d\varepsilon} = \frac{\phi^2}{1-\phi} \frac{\rho^2 \kappa (1-\kappa)}{\frac{G}{\tau_y} (1-\kappa) (\gamma_s^{(p)} - \gamma_u) + 1} G$

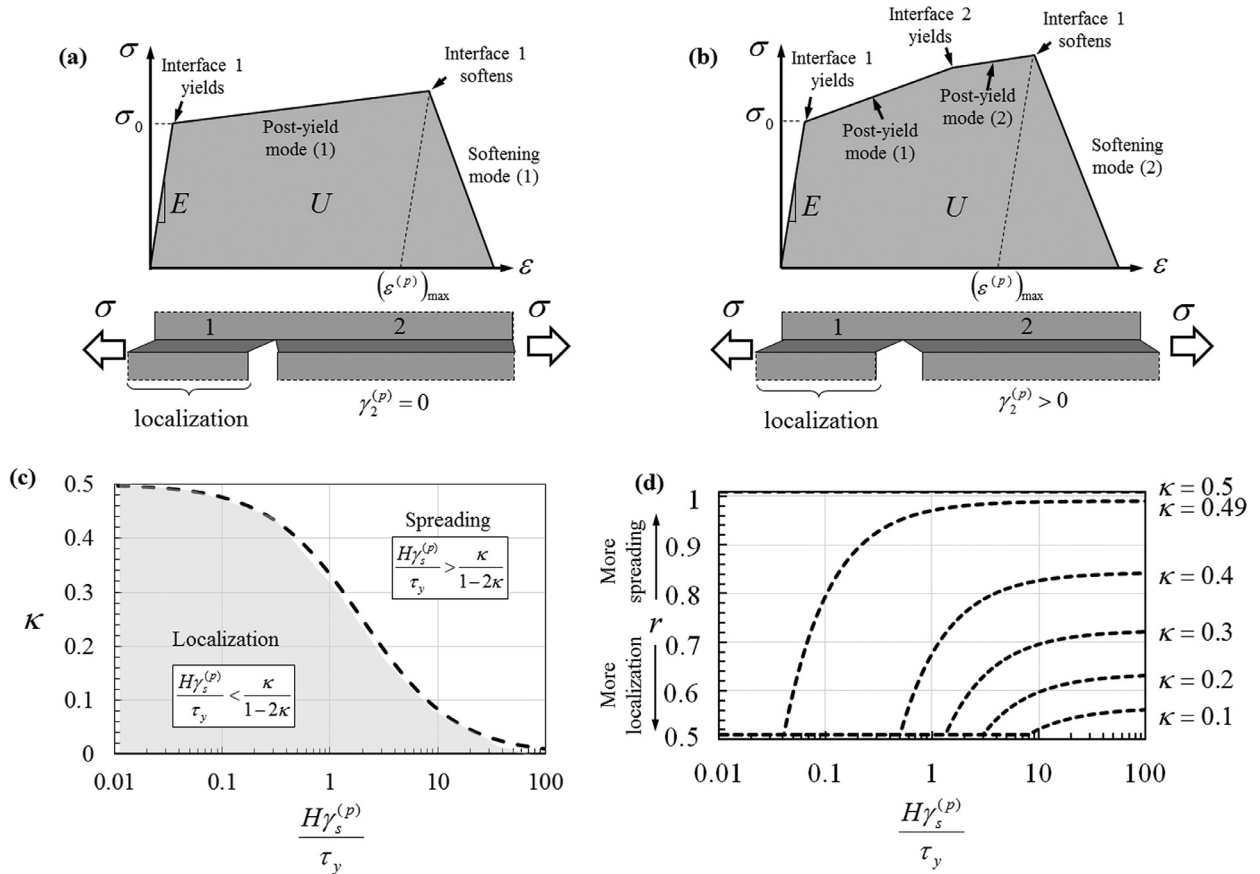


Fig. 3. Typical stress-strain curves for the cases of (a) localization (where only interface 1 yields) and (b) spreading of deformations (where interface 1 and 2 both yield). (c) Failure map which illustrates the condition for spreading vs. localization of deformation. Here κ can be interpreted as a measure of the microstructural defect, where $\kappa = 0.5$ corresponds to a perfect microstructure. (d) Spread of deformation, r , as a function of $H\gamma_s^{(p)}/\tau_y$ for different values of κ .

mode (2) when interface 1 eventually softens. Mode (2) is clearly more beneficial in terms of tensile strain at failure and energy absorption capabilities. The condition for mode (2) to occur over mode (1) is:

$$\frac{H\gamma_s^{(p)}}{\tau_y} > \frac{1-2\kappa}{\kappa} \quad (10)$$

We note that both high relative hardening at the interface H/τ_y and high deformability $\gamma_s^{(p)}$ promote mode (2). Eq. (10) also shows that high values of κ promote mode (2). In the absence of any hardening at the interface ($H=0$) mode (1) always prevails unless $\kappa = 0.5$. For a perfect microstructure where $\kappa = 0.5$, interface 1 and 2 are identical and in theory deform identically and simultaneously. Fig. 3c shows more features of Eq. (10), which can be interpreted as follows: the imbalance of overlap length between interfaces 1 and 2 ($\kappa < 0.5$) can be considered a defect which induces strain localization

and brittle failure. However, this effect can be offset by interfaces with high values of $H\gamma_s^{(p)}/\tau_y$. In terms of materials design, it is therefore important to choose an interface material with a high value of $H\gamma_s^{(p)}/\tau_y$, which will delay localization even in the presence of defects $\kappa < 0.5$. The higher the value of $H\gamma_s^{(p)}/\tau_y$, the more imperfections the microstructure can tolerate without localizing. Fig. 3c shows that increasing $H\gamma_s^{(p)}/\tau_y$ is the most effective in the range $H\gamma_s^{(p)}/\tau_y = 0.1 - 10$, where it decreases the “tolerable” defect from $\kappa \approx 0.47$ to less than 0.1. $H\gamma_s^{(p)}/\tau_y$ has little effect on localization behavior when it is too low ($H\gamma_s^{(p)}/\tau_y < 0.1$) or too high (beyond $H\gamma_s^{(p)}/\tau_y = 10$), however. To illustrate this result, we computed $H\gamma_s^{(p)}/\tau_y$ for the interfaces in nacre using literature values of $H = 11$ MPa, $\tau_y = 20$ MPa, $\gamma_s^{(p)} = 250$ nm/30 nm = 8.3 (Barthelat et al., 2007). Interestingly, these values give $H\gamma_s^{(p)}/\tau_y = 4.7$, which is within the range that most effectively delays localization.

We now examine the average RVE plastic strain as a measure of “ductility” in the material. More specifically, in the stable region of the material the maximum plastic strain occurs at the onset of localization and can be written:

$$(\varepsilon^{(p)})_{\max} = \kappa (\varepsilon_1^{(p)})_{\max} + (1 - \kappa) (\varepsilon_2^{(p)})_{\max} \quad (11)$$

At the shorter interface 1, the plastic strain at the interface has reached $\gamma_s^{(p)}$ so that:

$$(\varepsilon_1^{(p)})_{\max} = \frac{1}{\kappa \rho} \frac{1 - \phi}{\phi} \gamma_s^{(p)} \quad (12)$$

At interface 2 the plastic strain is:

$$(\varepsilon_2^{(p)})_{\max} = \frac{1}{(1 - \kappa) \rho} \frac{1 - \phi}{\phi} (\gamma_2^{(p)})_{\max} \quad (13)$$

With:

$$(\gamma_2^{(p)})_{\max} = 0 \text{ if } \frac{H\gamma_s^{(p)}}{\tau_y} \leq \frac{1 - 2\kappa}{\kappa} \text{ (mode (1))} \quad (14a)$$

$$(\gamma_2^{(p)})_{\max} = \frac{\kappa}{1 - \kappa} \left[\gamma_s^{(p)} - \frac{1 - 2\kappa}{\kappa} \frac{\tau_y}{H} \right] \text{ if } \frac{H\gamma_s^{(p)}}{\tau_y} > \frac{1 - 2\kappa}{\kappa} \text{ (mode (2))} \quad (14b)$$

Combining, (12) and (1) gives:

$$(\varepsilon^{(p)})_{\max} = \frac{1}{\rho} \frac{1 - \phi}{\phi} (\gamma_s^{(p)} + (\gamma_2^{(p)})_{\max}) \quad (15)$$

Remarkably, $(\varepsilon^{(p)})_{\max}$ does not depend on the overlap of the tablets κ . The perfect microstructure ($\kappa = 0.5$) serves again as a reference:

$$(\varepsilon_0^{(p)})_{\max} = \frac{2}{\rho} \frac{1 - \phi}{\phi} \gamma_s^{(p)} \quad (16)$$

We now introduce the ratio $r = \frac{(\varepsilon^{(p)})_{\max}}{(\varepsilon_0^{(p)})_{\max}}$, which can serve as a measure of the tensile “deformability” of the material compared to the perfect microstructure. Using Eq. (14), (15) and (16) gives:

$$r = \frac{1}{2} \text{ if } \frac{H\gamma_s^{(p)}}{\tau_y} \leq \frac{1 - 2\kappa}{\kappa} \text{ (mode (1))} \quad (17a)$$

$$r = \frac{1}{2} \left(1 + \frac{\kappa}{1 - \kappa} \left[1 - \frac{1 - 2\kappa}{\kappa} \frac{\tau_y}{H\gamma_s^{(p)}} \right] \right) \text{ if } \frac{H\gamma_s^{(p)}}{\tau_y} > \frac{1 - 2\kappa}{\kappa} \text{ (mode (2))} \quad (17b)$$

The lower bound for r using the small RVE is therefore 1/2 (in the second part of this article we will present models with larger number of tablets that produce much smaller values for r). In terms of optimizing material performance, r should be maximized because it promotes large deformations that can accommodate and limit the effects of stress concentrations, imparting the material with damage tolerance. Large deformations also promote energy absorption (Barthelat, 2014) and toughness (Barthelat and Rabiei, 2011). Fig. 4c shows that there are two ways to increase r : (i) use microstructures which are as close as possible to perfect (i.e. κ as close to 0.5 as possible) and (ii) use interfaces with high values of $H\gamma_s^{(p)}/\tau_y$. As a last step for the analysis of the small RVE, we computed the energy absorbed in the material up to the softening point, normalized again by the energy absorption for a perfect microstructure:

$$\frac{U}{U_0} = \kappa + (1 - \kappa) \frac{\left(1 + \frac{1}{2} \frac{H\gamma_s^{(p)}}{\tau_y} \frac{(\gamma_2^{(p)})_{\max}}{\gamma_s^{(p)}} \right)}{\left(1 + \frac{1}{2} \frac{H\gamma_s^{(p)}}{\tau_y} \right)} \frac{(\gamma_2^{(p)})_{\max}}{\gamma_s^{(p)}} \quad (18)$$

With $(\gamma_s^{(p)})_{\max}$ given by Eq. (14). Eq. (18) is illustrated in Fig. 4d. The slightest deviation from a perfect microstructure decreases U/U_0 significantly, but these morphological defects can be compensated by using high values of $H\gamma_s^{(p)}/\tau_y$ at the interface.

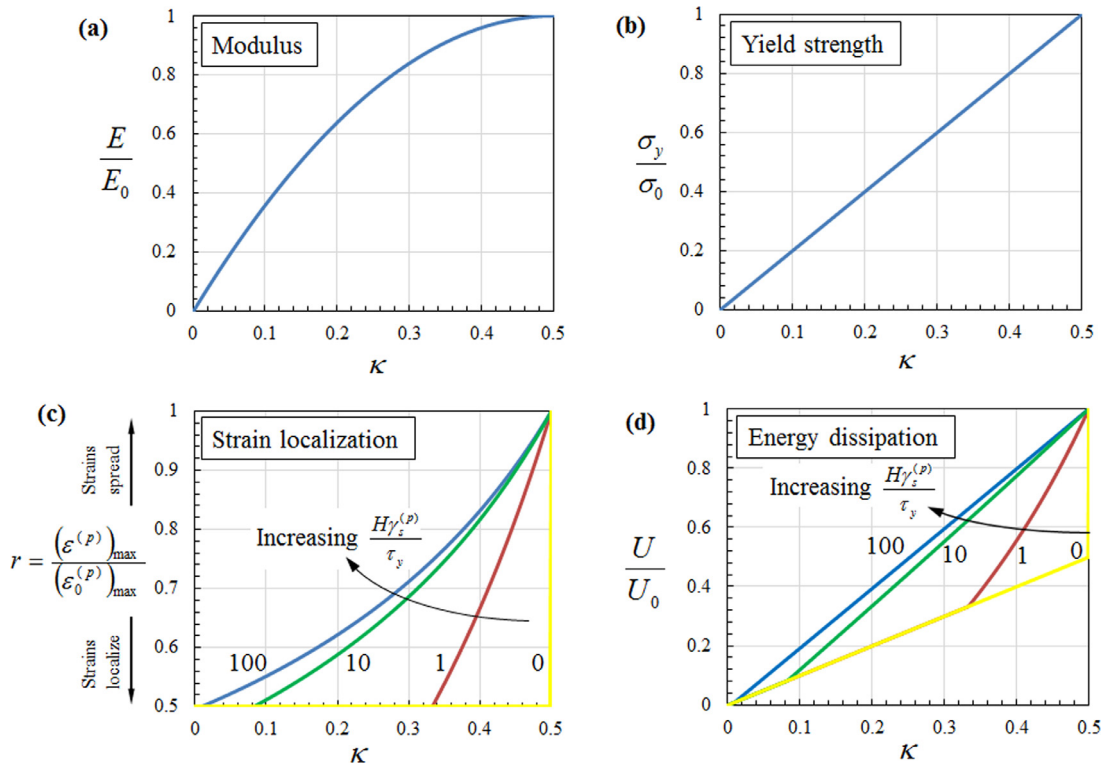


Fig. 4. Key properties for the RVE in tension as functions of κ and normalized by the properties of a “perfect” microstructure ($\kappa = 0.5$, index “0”): (a) modulus, (b) strength, (c) maximum tensile plastic strain, (d) energy dissipation.

3. Discrete element models

The small RVE considered so far provides useful insights into strain localization and how it can be delayed. However, in this model the defects are simply modeled as an “unbalance” of overlap lengths through a single parameter κ . This does not capture more complex, longer range deformation mechanisms associated with the presence of local defects and statistical variations within the microstructure. To capture these effects the small RVE model must be replaced by a much larger “statistical volume element” (SVE) that contains a large number of tablets and can therefore capture finite mesoscale statistical scatter within a large volume (Ostoja-Starzewski, 2006).

In this work, we used a discrete element approach to lower the computational cost of modeling large volumes of staggered composites. Our DEM approach assumes that (i) each tablet is represented by a “node” that has only one degree of freedom (displacement along the direction of pulling), and (ii) the tablets (nodes) are connected to their neighboring tablets with nonlinear springs (Fig. 5a). The spring behavior was governed by the shear stress-strain curve shown on Fig. 2b, multiplied by the length of the interface. As in conventional finite elements, an element stiffness matrix was defined for each interface and was assembled into a global stiffness matrix. We used displacement controlled boundary conditions on the model: The left boundary of the model was held fixed and a uniform displacement was applied on the right boundary. The displacement was ramped linearly at each loading step. As expected the model behaved elastically and linearly until the first interface yielded. The rest of the simulation was then performed with a standard Newton–Raphson method (Press et al., 1987; Ghaboussi and Barbosa, 1990). The inherent hardening behavior implemented at the interfaces, made an increasing number of elements yield, until eventually some of these elements entered the softening region. Unloading of the interfaces was captured by storing the maximum deformation experienced at each interface. Any deformation beyond that maximum value would follow the piecewise linear cohesive law described above. Deformations below the maximum deformation in the history of the interface corresponded to unloading. In that case, the deformation was simply proportional to the shear modulus of the interface G . This unloading scheme corresponded to interfaces that accumulate residual deformations past the initial yield point. Model generation, simulation and post-processing were all implemented in Matlab (Mathews and Fink, 2004). The DEM method implemented was validated using the small 14 tablet model shown in Fig. 5a and b. The results from our DEM code were in perfect agreement with the analytical stress-strain curves presented in the previous section.

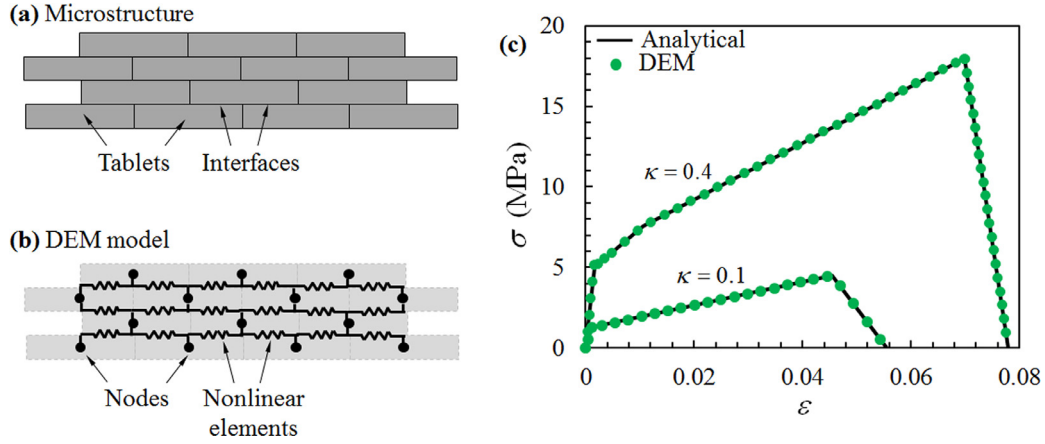


Fig. 5. Validation of the DEM model (a) a 14 tablet model and (b) corresponding DEM model with rigid tablets and a nonlinear spring at each interface. microstructure and (b) its discrete element mesh representing a brick and mortar structure. Here tablets and their interfaces are represented by nodes and nonlinear elements respectively. (c) Comparison between the analytical solution and DEM results for the small RVE. The agreement was perfect for all parameters (for this figure, $G = 100$ MPa, $H = 6$ MPa, $\tau_y = 3.5$ MPa, $\gamma_s^{(p)} = 1.5$, $\gamma_u = 2$, $\rho = 4$, and $\kappa = 0.1$ & 0.4).

3.1. Construction of large DEM models

Biological and synthetic bioinspired staggered composites show statistical variations in their microstructures (variation in tablet size and arrangement), as well as their constituent properties (heterogeneous tablet and interfacial materials). To capture the impact of these variations on mechanical performance, we generated large statistical volume elements (SVEs) based on the DEM approach. In this work, we assumed that the properties of the interfaces were uniform within each model and introduced statistical variations on the microstructure. These variations translated in non-homogenous overlap length between tablets, which in turn resulted in local variations in interface stiffness, strength and ductility. Another way of introducing statistics into the model is by varying the interface cohesive law which is beyond the scope of this paper. In this work, we chose to focus on microstructural variations and assumed all interfaces properties were identical, which is more representative of bio-inspired synthetic nacles (uniform materials, non-uniform microstructures). First, an array of N_x by N_y tablets was constructed from tablets with aspect ratio of $\bar{\rho}$ (mean aspect ratio). Every other layer was offset by a distance $\kappa \bar{\rho}$, where κ is the “overlap ratio” defined above. Statistical variations were then introduced in the microstructure by disturbing the position of the nodes by a distance $\Delta x_{i,j}$, a realization of a statistical distribution with mean of zero. In this work we used a normal distribution, because the aspect ratio of natural nacre was found to follow this specific type of distribution (Barthelat et al., 2007; Rabiei et al., 2010; Song et al., 2003; 2011). Normalizing all dimensions by the thickness of the tablets, the positions of the nodes in the x-y coordinate system is given by:

$$\begin{cases} \frac{x_{i,j}}{t} = \frac{d_j}{t} + (i-1)\bar{\rho} + \frac{\Delta x_{i,j}}{t} \\ \frac{y_{i,j}}{t} = j-1 \end{cases} \quad (19)$$

Where $1 \leq i \leq N_x$ and $1 \leq j \leq N_y$. The stagger distance was $d_j = 0$ for j even and $d_j = (1 - \kappa)\bar{\rho}$ for j odd. The aspect ratio of each tablet was then given by:

$$\rho_{i,j} = \frac{1}{2t} (x_{i+1,j} - x_{i-1,j}) \quad (20)$$

The overlap ratio of the n^{th} interface (κ_n) between the tablets i and j is given by:

$$\kappa_n = \frac{(x_{i+1,j} - x_{i,j+1})}{(x_{i+1,j} - x_{i-1,j})} \quad (21)$$

With this description of the microstructure, the nodes were not necessarily at the center of the tablets. From the property of the standard deviation and Eqs. 20 and 21, the standard deviation in the aspect ratio ($\Delta\rho$), overlap length ($\Delta\kappa$) and tablet center point shift can be related:

$$\Delta\rho = \sqrt{\frac{1}{2} \left(\frac{\Delta x_{i,j}^2}{t^2} \right)} \quad (22)$$

and

$$\Delta\kappa = \exp(\sqrt{2}[\ln(\sqrt{2}\Delta x_{i,j})]). \quad (23)$$

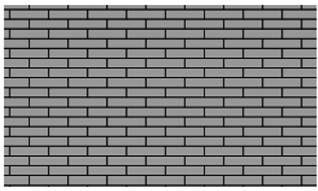
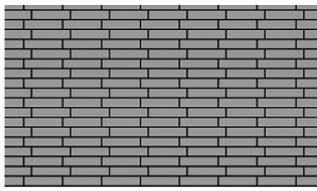
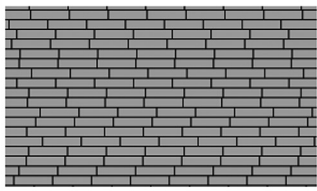
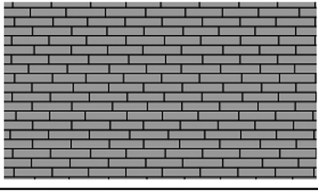
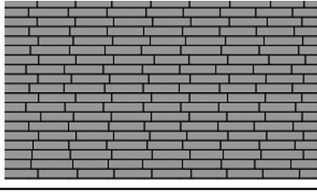
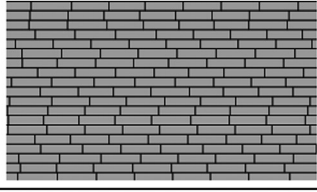
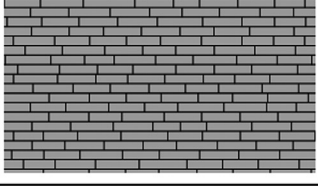
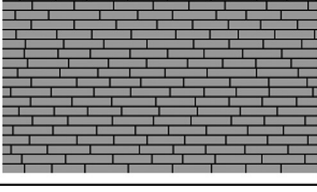
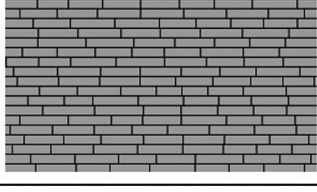
	Running bond ($\kappa=0.5$)	Columnar nacre ($\kappa<0.5$)	Sheet nacre
Uniform tablets ($\Delta\rho/\bar{\rho} = 0.0$)			
Nonuniform tablets ($\Delta\rho/\bar{\rho} = 0.025$)			
Nonuniform tablets ($\Delta\rho/\bar{\rho} = 0.125$)			

Fig. 6. The three types of microstructures explored in this study: Running bond, columnar nacre and sheet nacre. The effects of statistical variations on the microstructure are shown for three different standard deviations.

In the models we set the standard deviation of the normalized position $\frac{\Delta x_{i,j}}{t}$ to $\sqrt{2}\Delta\rho$, which resulted in tablets with an average aspect ratio $\bar{\rho}$ and standard deviation $\Delta\rho$ (Fig. 7a). We explored the effects of $\Delta\rho/\bar{\rho}$ in the range 0 to 0.125, which is in the order of the statistical variations measured on natural nacre (Rabiei et al., 2010). $\Delta\rho/\bar{\rho}$ can be much higher for synthetic nacre-like materials (Bonderer et al., 2008; Deville et al., 2006), but we did not explore $\Delta\rho/\bar{\rho}$ values higher than 0.125 because wide normal distributions could produce realizations of ρ that were negative. To prevent such case the tail of the normal distribution was cropped to ensure $\rho > 0$ for all realization of ρ . This precaution did not produce any significant bias on the results, provided that the standard deviation was within the limit $\Delta\rho/\bar{\rho} < 0.125$ (This range of statistical variations was sufficient to generate significant changes in the mechanical response of the models). This procedure was used to produce three types of microstructures (Fig. 6): (i) “running bond” where $\bar{\kappa} = 1/2$, (ii) “columnar nacre” where $0 < \bar{\kappa} < 1/2$ and (iii) “sheet nacre” microstructures where there were no correlation of position across the layers of tablets (the stagger of each layer was assigned a random value d_j between 0 and $\bar{\rho}$, following a uniform probability distribution). Fig. 6 shows the effect of statistics on the each of these three types of microstructure.

Once the position of the nodes was established, overlapping tablets were detected, and the overlap length was computed to populate a connectivity table. The interface of each overlapping region was then modeled with one DEM element whose behavior was governed by the cohesive law and by the length of the overlapping interface. Fig. 7 shows a model with a running bond microstructure with $\Delta\rho/\bar{\rho} = 0.025$. In this case, the size of the model was 60×60 tablets (3600° of freedom). The cohesive law in this example had the characteristic $H\gamma_s^{(p)}/\tau_y = 0.1$ (Fig. 7a).

Fig. 7(b) shows the tensile stress-strain curve obtained from this model. The response is linear up to about 16 MPa (at 0.5% strain). A yield point is followed by strain hardening, which ends by a slight decrease of stress at which point the simulation fails to converge. Qualitatively, the shape of the stress strain curve was consistent with experimental results on natural nacre shells (Barthelat et al., 2007). Using interface parameters closer to natural nacre produced realistic stress-strain curves which captured σ_y and H for natural nacre. However, the model overestimated E , σ_s , and ε_s , possibly because of our assumption of rigid tablets, the two-dimensional approximation as well as the presence of relatively large defects in natural nacre. Fig. 7c shows snapshots of the model at different points on the stress strain curves. We used color code for the interfaces to indicate if they are elastic (thin black line), yielding (yellow), softening (red) or unloading from a yielded state (grey). Under tension, the shortest interfaces yield first, generating an interspersed distribution of isolated yielding interfaces that grows in density as the load increases. Interestingly this cloud of yielded interfaces is well developed even in the linear region of the stress-strain curve (snapshot 2). In this case, the density of yielded interfaces increases rapidly in the hardening region, and almost all the interfaces yield (snapshot 3). However, this process is interrupted by a localization region (snapshot 4) that propagates across the direction of pulling and eventually across the entire model (snapshot 5). On either side of the softening region, the interfaces unload as the local stress decreases. At this point the model ceased to converge because of elastic snapback, a known issue with the Newton Raphson method (the softening branch maybe captured using damping at the interface (Gao and Bower, 2004) but we have not pursued this route since we were only

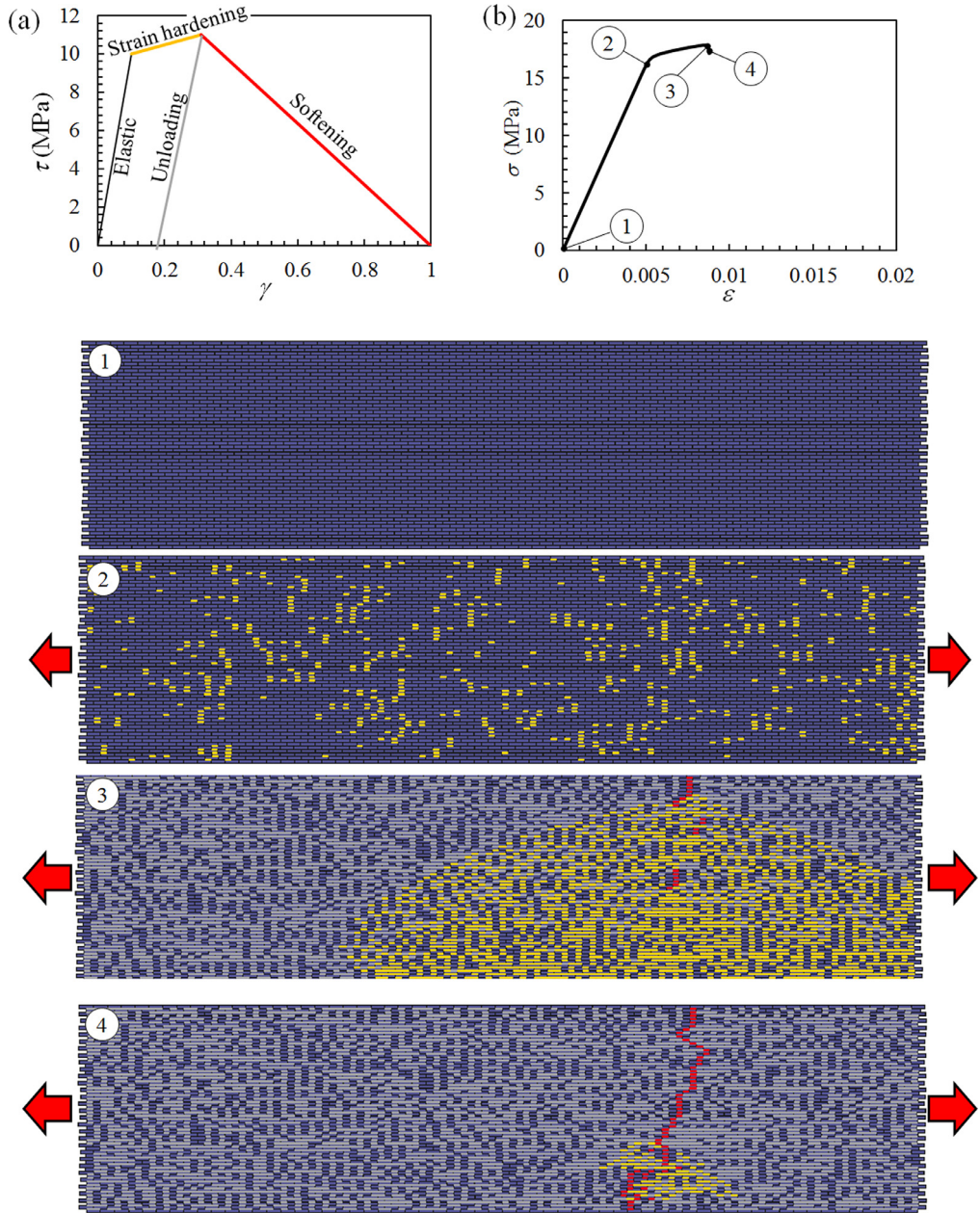


Fig. 7. Example of a 60×60 DEM model under uniaxial loading condition. Running bond with $\Delta\rho/\bar{\rho} = 0.025$ and (a) cohesive law with $H\gamma_s^{(p)}/\tau_y = 0.1$ (b) tensile stress-strain curve produced by this model and (c) corresponding sequence of deformation showing small amount of yielding interspersed in the model, followed by widespread yielding and by a localization, and finally softening and unloading of the rest of the material. This model produced a localization ratio $r = 0.15$.

interested in capturing the onset of localization and failure for each microstructure). The “ductility” of the microstructure was characterized using these large models, where Eq. (15) becomes:

$$\varepsilon^{(p)} = \frac{2}{N\bar{\rho}} \frac{1-\phi}{\phi} \sum_{n=1}^N \gamma_n^{(p)} \quad (24)$$

where $\gamma_n^{(p)}$ is the plastic shear strain at interface n and N is the total number of interfaces. Note that $\varepsilon^{(p)}$ can also be obtained from the tensile stress-strain curve.

$$(\varepsilon_0^{(p)})_{\max} = \frac{2}{\bar{\rho}} \frac{1-\phi}{\phi} \gamma_s^{(p)} \quad (25)$$

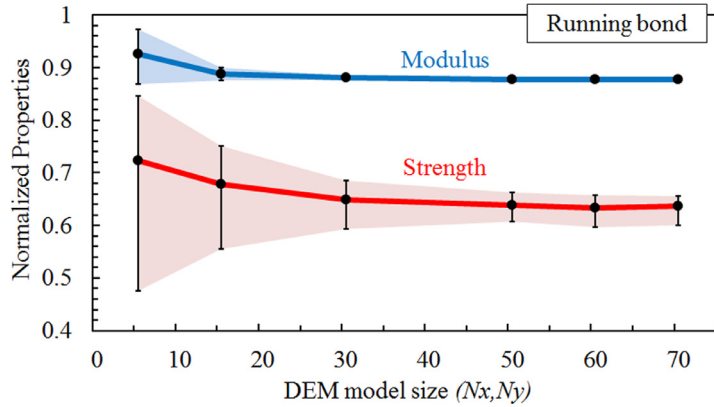


Fig. 8. Effect of SVE size on the overall modulus and strength for running bond. In this case ($\Delta\rho/\bar{\rho} = 0.05$ and $N_x = N_y$), convergence is achieved at an SVE size of 60×60 tablets. While the variations in modulus almost disappear for large SVE, there are still significant variations in strength even after convergence. These variations are inherent to the material and are SVE-size independent. (for this figure $\kappa = 0.5$, $G = 100$ MPa, $H = 0.8$ MPa, $\gamma_s^{(p)} = 2$, $\gamma_u = 3$, and $\tau_y = 1.3$ MPa).

The normalized maximum plastic strain is then:

$$r = \frac{(\varepsilon^{(p)})_{\max}}{(\varepsilon_0^{(p)})_{\max}} = \frac{\frac{1}{N} \sum_{n=1}^N \gamma_n^{(p)}}{\gamma_s^{(p)}} \quad (26)$$

The example shown in Fig. 7 produced $r=0.15$, a relatively large value which reflects the ductility of this material. As described in the rest of this article, varying the type of microstructure, its statistical variation, and the characteristics of the cohesive law (parameter $H\gamma_s^{(p)}/\tau_y$) had a profound effect on the distribution, shape, and extent of the yielded regions prior to localization. In turn, these different behaviors had an effect on the strength and deformability of the microstructure. To assess these effects with confidence, we had to ensure that the results were independent of the model size ($N_x \times N_y$) (Ostoja-Starzewski, 2006; Gitman et al., 2007). To assess the effect of model size on predicted properties, we generated a series of “running bond” models of increased size with $N_x=N_y=5, 15, 30, 50, 60$, and 70 . For each of these sizes, 100 realizations of the microstructure were automatically generated and run. Fig. 8 shows the effect of model size on the macroscopic modulus and strength for the staggered composites (using $\Delta\rho/\bar{\rho} = 0.05$, $\kappa = 0.5$, $G = 100$ MPa, $H = 0.8$ MPa, $\gamma_s^{(p)} = 2$, $\gamma_u = 3$, and $\tau_y = 1.3$ MPa). Modulus and strength were normalized by the “perfect” small RVE microstructure values E_0 and σ_0 , respectively, computed from the cohesive law and $\bar{\rho}$. Fig. 8 shows that smaller models produced more variations in predicted strength and modulus properties across realizations. Increasing the size of the model produced more consistent values for these properties as the size converged to a “statistical volume element” (SVE) sufficiently large enough to accurately reflect the effects of statistics on the average properties. We also verified that the results are not dependent on the boundary conditions by running models under both displacement and traction-based loading conditions. Ten realizations of the model with 60×60 tablets (the point at which the behavior is not affected by further increase in the RVE size for the parameters used here (Fig. 8)) were developed and analyzed. The results show that changing boundary condition has less than 2% effect on the modulus. Moreover, we found that there is less than 1.5% difference between the left and right hand sides of the Hill–Mandel condition ($\bar{\sigma} : \bar{\varepsilon} = \bar{\sigma} : \bar{\varepsilon}$) for the ten realizations of the model with 60×60 tablets. Therefore, our boundary condition and model size is consistent with the Hill–Mandel condition (Ostoja-Starzewski, 2006; Nguyen et al., 2012; Dalaq et al., 2013). Fig. 8 shows that the deviation in modulus decreases as the size of the model is increased. The statistics in the microstructure also makes the material slightly less stiff compared to the perfect microstructure ($\bar{E} = 0.9E_0$). The variation of strength also decreased as the model increased, but this statistical variation never completely vanished. In the SVE range, the strength is governed by “weakest link” statistics which cannot be eliminated by increasing the size of the model. Even for large models, these variations in strength are also observed in other types of SVEs (Lu and Bhattacharya, 2005; Kanit et al., 2003). Therefore, they are inherent to the microstructure and are similar to Weibull statistics used on brittle materials. The exact distributions of modulus and strength are explored further in the remainder of this article. Fig. 8 also shows that the effect of statistics is much more pronounced on average strengths than on average modulus. For this case, we obtained $\bar{\sigma} \approx 0.6\sigma_0$. Convergence studies on model size were performed for each type of microstructure, so that the models presented below are all model size independent. Typical SVE sizes ranged from 60×60 to 120×120 tablets.

3.2. Large DEM models, results

The large DEM models retain the expected effect of the cohesive law parameters on modulus, strength and deformability. For example, increasing the shear modulus G increases the modulus E , increasing τ_y increases the yield strength in tension,

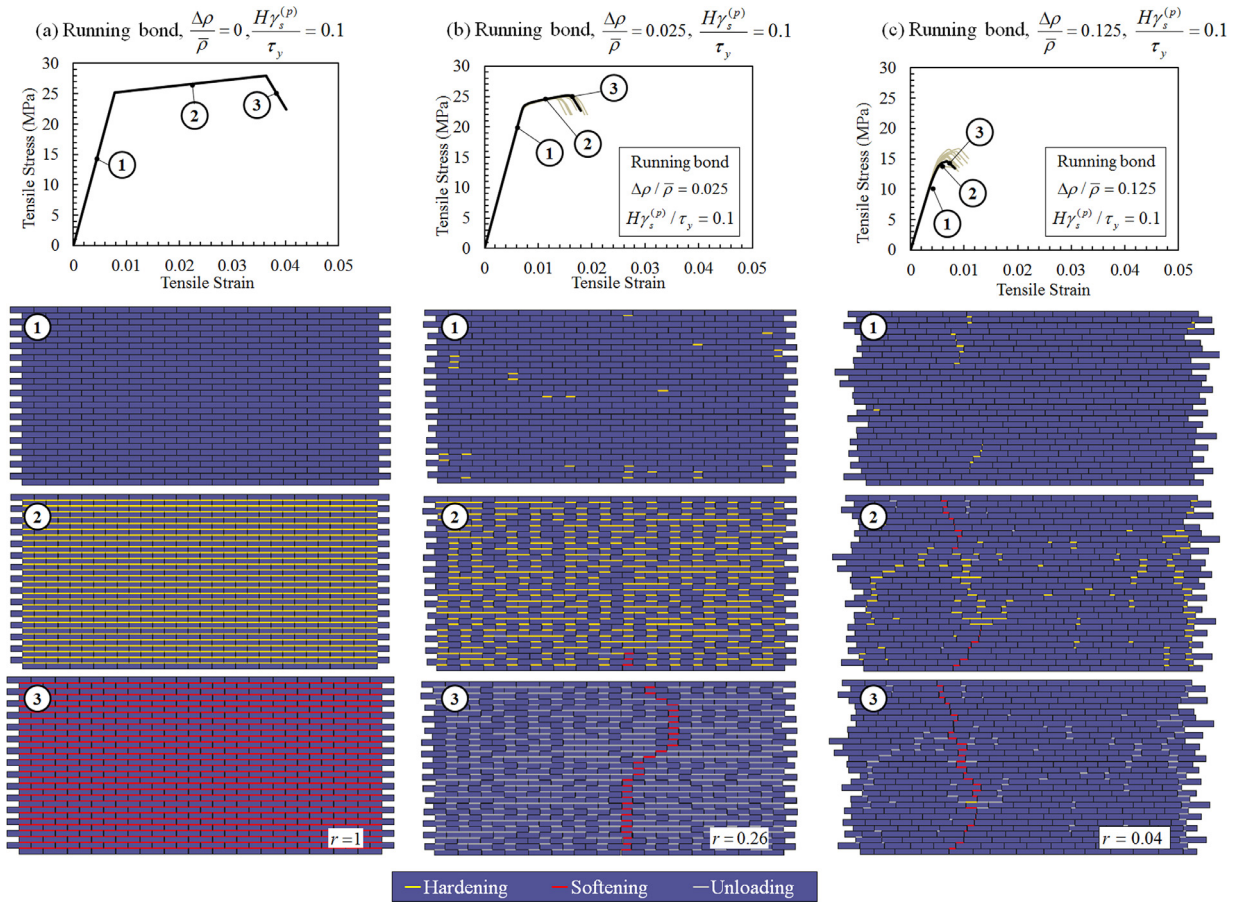


Fig. 9. Effect of statistical variations on stress-strain curve and failure mechanism (small 30×15 models are shown for illustration). All models are of the “running bond” type, with $H\gamma_s^{(p)}/\tau_0 = 0.1$. (a) $\Delta\rho/\bar{\rho} = 0$ (perfect microstructure, no statistics); (b) $\Delta\rho/\bar{\rho} = 0.025$; (c) $\Delta\rho/\bar{\rho} = 0.125$. For each case, the computed value of r is indicated on snapshot#3.

and increasing $\gamma_s^{(p)}$ increases the tensile strain at failure for the material. Here we focus on the effect of the cohesive law, microstructure type, and statistics on the ability to delay localization (as measured by the ratio r defined above). The parametric studies we performed on the large SVE by varying H , $\gamma_s^{(p)}$, and τ_y confirmed that the contribution of the cohesive law to the r value is also governed by the single parameter $H\gamma_s^{(p)}/\tau_y$. With this result in hand, we examine the role of statistics, the value of $H\gamma_s^{(p)}/\tau_y$, and the microstructure type on the stress-strain response and the r value. Fig. 9 shows the effect of statistics with three models, all of the “running bond” type and with $H\gamma_s^{(p)}/\tau_y = 0.1$. The models are relatively small (30×15) for illustration purposes, but their behavior is representative of larger SVEs. The perfect microstructure with no statistics (Fig. 9a, $\Delta\rho/\bar{\rho} = 0$) is identical to what is predicted by the small RVE. Every interface yields simultaneously in the model and at a single yield point on the tensile stress-strain curve. The interfaces also soften simultaneously, so that stress strain curve directly reflects the cohesive law used at the interface. The tensile strain at failure is relatively large because every interface yields in unison and contribute to the large deformations. In this perfect microstructure there is no localization, and $r = 1$. Fig. 9b shows the effect of introducing a slight amount of statistics ($\Delta\rho/\bar{\rho} = 0.025$). In this case, a few weak interfaces (i.e. those with shorter overlap lengths) start yielding even in the linear region of the stress-strain curve. As the stress increases, the density of the yielded interfaces increases and some of them coalesce, generating enough nonlinear deformations to form a yield point on the stress-strain curve. Since the statistical variations introduce “weakest links” in the model, the strength of the model with statistics is lower than the perfect model. Snapshot 2 also shows a localization band that initiates at the lower edge of the model. While the softening localization band propagates, the local stress decreases which interrupts the formation of new yielding interfaces. The localization band eventually coalesces across the model (snapshot 3) which precipitates failure, so that the value of r is greatly reduced: $r = 0.26$. The localization band is jagged due to statistics as well as the combined shear and tensile stresses in its vicinity, which trigger a “stair” type of failure (Rabiei et al., 2010). Finally, Fig. 9c shows a case with large statistical variations ($\Delta\rho/\bar{\rho} = 0.125$). The yield strength is greatly reduced because the weakest link in the microstructure is made even weaker by the statistics. The density of yielding is very low and rapidly interrupted by the localization. The strain at failure is small and the material and r

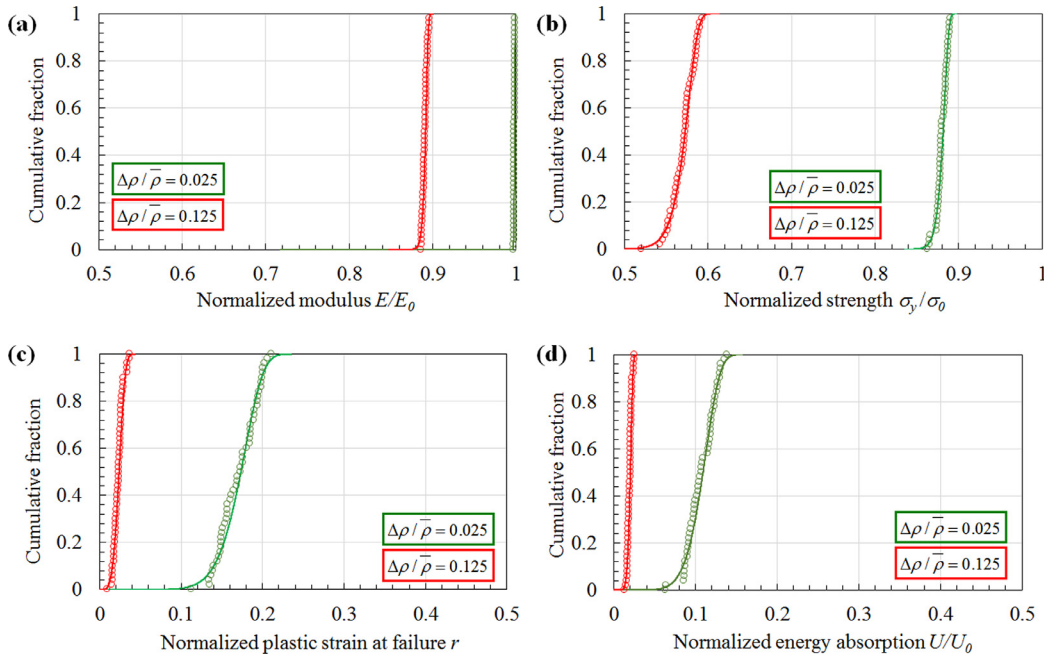


Fig. 10. Cumulative distribution of (a) normalized modulus, (b) normalized strength, (c) normalized ductility, (d) normalized energy absorption. All models are of the “running bond” type, with $H\gamma_s^{(p)}/\tau_0 = 0.1$ and are (60×60) and (120×120) tablet SVE models with two different statistical distributions of $\Delta\rho/\bar{\rho} = 0.025$ and $\Delta\rho/\bar{\rho} = 0.125$, respectively. (50 realizations were evaluated for each statistics).

becomes very small: $r = 0.04$. Fig. 10 shows the effect of statistics on materials properties. While the effect is minimal on modulus, statistical variations in the microstructure greatly decrease strength, ductility r , and in turn energy absorption. $\Delta\rho/\bar{\rho} = 0.025$ produces seemingly negligible variations in the microstructure (Fig. 6), but these small variations decrease the energy absorption capabilities of the material by as much as 90%. These examples clearly demonstrate that while a cohesive law with large deformations may appear to lead to high performance with a small RVE, statistical variations in microstructure can precipitate failure and embrittle the material.

The next set of examples shows the effect of $H\gamma_s^{(p)}/\tau_y$ on mechanical response (Fig. 11). All models are of the “running bond” type, with moderate statistical variation in microstructure ($\Delta\rho/\bar{\rho} = 0.025$). All models shown are from one realization of the statistical distribution (i.e. the microstructures in Fig. 11a–c were strictly identical). Low values of $H\gamma_s^{(p)}/\tau_y$ ($H\gamma_s^{(p)}/\tau_y = 0.01$) produce a very brittle response, with very low r ($r = 0.03$). Increasing $H\gamma_s^{(p)}/\tau_y$ to 0.1 increases the deformability of the microstructure and produces more yielding and higher r ($r = 0.26$, Fig. 11b). Finally increasing $H\gamma_s^{(p)}/\tau_y$ to an even larger value ($H\gamma_s^{(p)}/\tau_y = 1$) enables the yielding of all the interfaces available, which produces a long yielding region with strain hardening and a high r value ($r = 0.73$, Fig. 11c). These examples clearly show how $H\gamma_s^{(p)}/\tau_y$ can be increased to delay localization, spread inelastic deformations and offset the negative effects of statistical variations in the microstructure.

Finally, Fig. 12 shows the effects of microstructure type on the stress-strain curve and deformation patterns. The columnar nacre we chose for this example had an average overlap of $\kappa = 0.25$, which is half of the average overlap for the running bond. As a result, the strength of the columnar nacre was only about 50% of the strength of the running bond (for which $\kappa = 0.5$). The columnar nacre was also more brittle, with $r = 0.13$ (also about half of the r value for the running bond). Snapshot 2 of Fig. 12b shows clearly that the smaller deformations of the columnar nacre are due to the yielding being confined to the smaller overlapping regions. The localization band is also straight, following a column of tablets. Fig. 12c shows that the strength and brittleness of sheet nacre was similar to that of the columnar nacre. The average overlap is $\kappa = 0.25$ (the same values as the one used for the columnar nacre) with a uniform statistical distribution of overlap. The yielding and localization bands also seek the weak regions, i.e. smallest overlaps, but unlike columnar nacre, sheet nacre produces yielding and softening region which are highly jagged.

A summary of the effects of randomness on properties and for different microstructures is given on Fig. 13. In all cases, random perturbations of the microstructure have only modest impacts on modulus (Fig. 13a). The effect on strength is more severe: within the range of statistics we explored, up to 40–60% of the strength was lost due to statistical variations for all types of microstructures (Fig. 13b). The most severe negative effects were on plastic strain at failure (Fig. 13c) and on energy absorption (Fig. 13d). Relatively small random variations ($\Delta\rho/\bar{\rho} = 0.05$) precipitate strain localization and decrease r by ~ 70 –80%, while energy absorption decreases by ~ 97 –99% for all microstructures. The larger statistical variations we

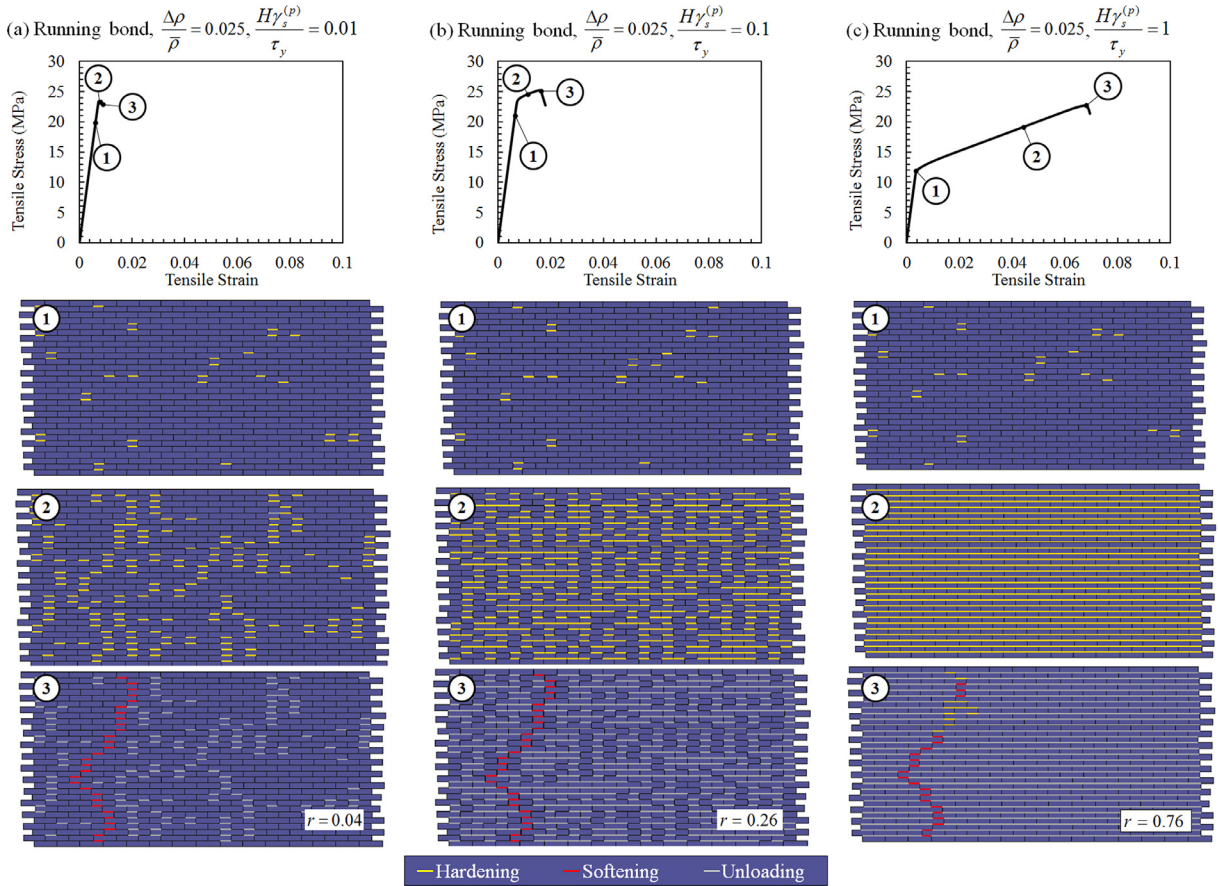


Fig. 11. Effect of the cohesive law on stress-strain curve and failure mechanism (small 30×15 models are shown for illustration). All models are of the “running bond” type, with $\Delta\rho/\bar{\rho} = 0.025$: (a) $H\gamma_s^{(p)}/\tau_0 = 0.01$ (b) $H\gamma_s^{(p)}/\tau_0 = 0.1$; (c) $H\gamma_s^{(p)}/\tau_0 = 1$. For each case, the computed value of r is indicated on snapshot#3.

explored here led to further decrease in r and U/U_0 . These statistical variations seem large, but they are still smaller than what is observed in most modern bio-inspired nacre-like composites.

Finally, Fig. 14 shows a summary of the effect of $H\gamma_s^{(p)}/\tau_y$ on the strain at failure r , for each of the three microstructures we explored and for different statistical distributions. For all cases, higher values of $H\gamma_s^{(p)}/\tau_y$ delay localization and consequently increases r . However, it also appears that increasing $H\gamma_s^{(p)}/\tau_y$ is only effective within the range 0.1 to 10. Values of $H\gamma_s^{(p)}/\tau_y$ smaller than 0.1 or greater than 10 have little effects on delaying localization.

4. Summary and conclusions

The staggered architecture is prominent in biological materials such as nacre, bone, tooth enamel, and spider silk. This particular architecture offers attractive combinations of strength, toughness and energy absorption, and it is now serving as model for the design and fabrication of modern composite materials. In this study, we examined the effect of random variations in microstructures, interface properties, and type of microstructures using small RVE models and large SVE models based on discrete element modeling. The main conclusions are summarized below:

- (1) The effects of imperfections in the staggered structure can be captured using small RVEs with an imbalance in overlap lengths. Large discrete element models can capture the effects of statistical variations in microstructure in a more comprehensive and realistic fashion.
- (2) Statistical variations have a modest effect on stiffness, but a more pronounced negative effect on strength. Statistical variations have a very large negative impact on ductility and energy absorption. Seemingly small statistical perturbations ($\Delta\rho/\bar{\rho} = 0.025$) from the perfect microstructure can decrease energy absorption capabilities of the material by up to 95%.
- (3) The negative effects of microstructure can be partially offset by using interfaces with high deformability and strain hardening. More specifically, the interface parameter $H\gamma_s^{(p)}/\tau_y$ must be maximized within the range 0.1 to 10 to delay

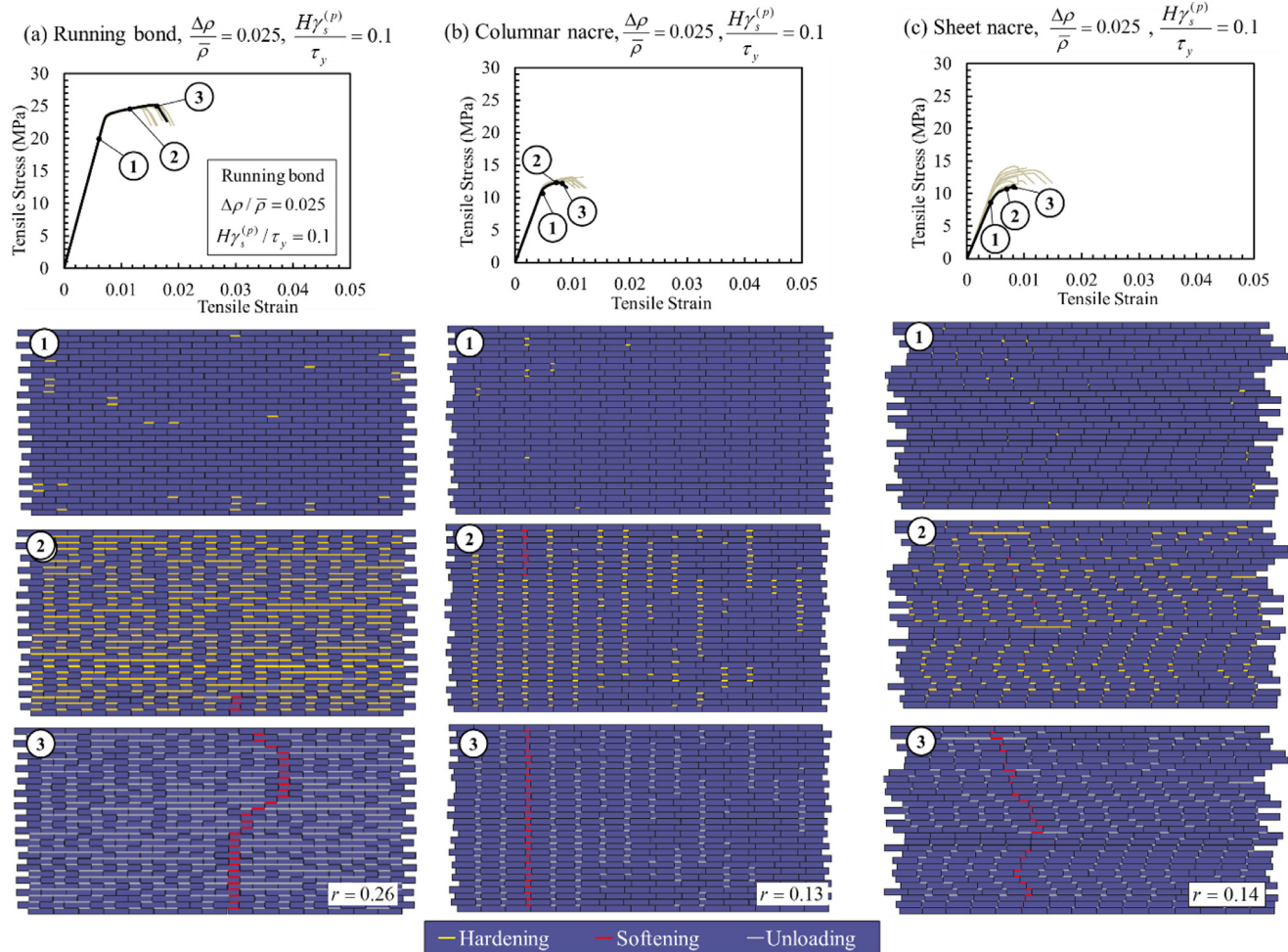


Fig. 12. Effect of the microstructure type on stress-strain curve and failure mechanism (small 30×15 models are shown for illustration). All models are built with $\Delta\rho/\bar{\rho} = 0.025$, and a cohesive law $H\gamma_s^{(p)}/\tau_y = 0.1$: (a) Running bond; (b): Columnar nacre; (c): Sheet nacre. For each case, the computed value of r is indicated on snapshot #3.

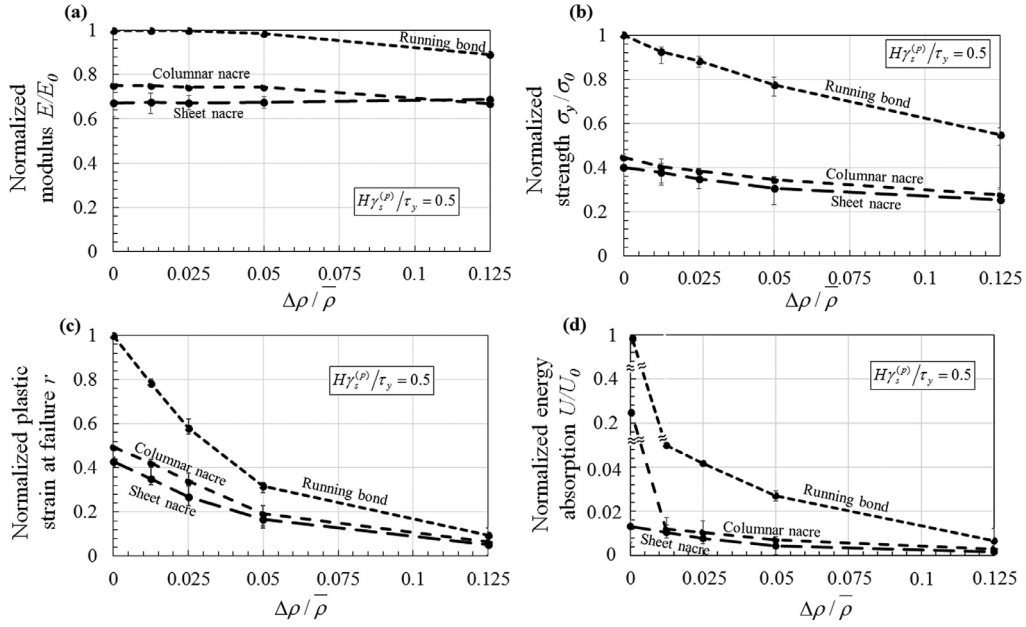


Fig. 13. Normalized properties as functions of relative standard deviation in the microstructure for $H\gamma_s^{(p)}/\tau_y = 0.5$ and for running bond, columnar nacre and sheet nacre: (a) modulus; (b) strength (c) strain at failure r and (d) energy absorption.

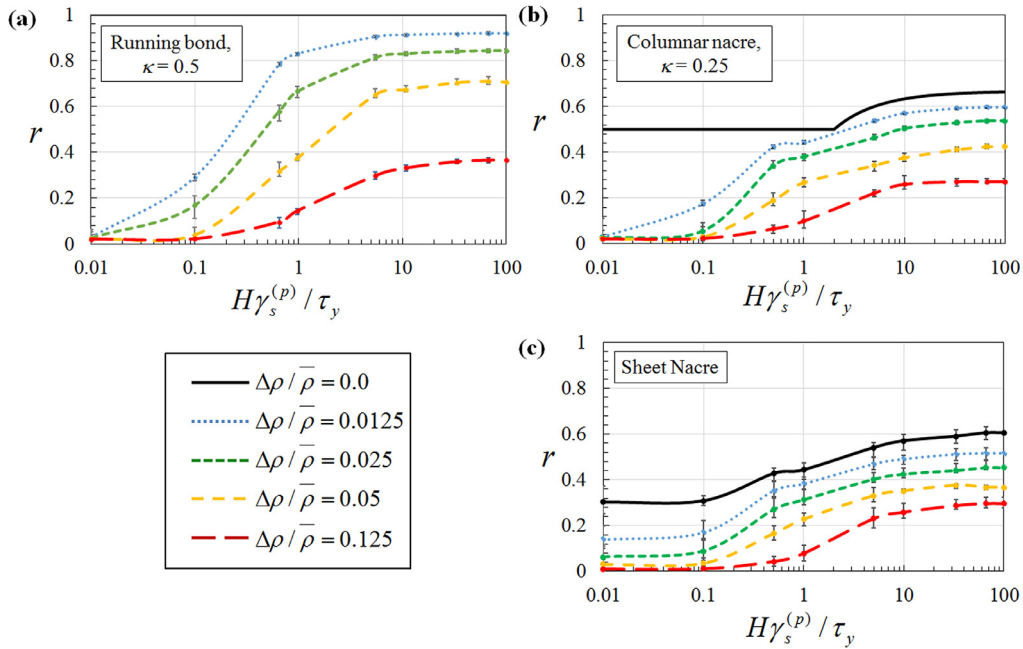


Fig. 14. Effect of $H\gamma_s^{(p)}/\tau_y$ on the strain at failure r , for each of the three microstructures we explored and for different statistical distributions: (a) running bond, (b) columnar nacre and (c) sheet nacre.

localization. Values of $H\gamma_s^{(p)}/\tau_y$ smaller than 0.1 or greater than 10 have little effects on performance. Interestingly, for the interfaces in nacre, $H\gamma_s^{(p)}/\tau_y = 4.7$ which is within that “optimal” range.

- (4) Different arrangements of tablets (running bond or sheet) produce different values of modulus and strength, but display the same behavior and response to $H\gamma_s^{(p)}/\tau_y$ in terms of localization.
- (5) The discrete element model proved to be a valuable tool for the modeling of random staggered composites, where the mechanical response is governed by interfaces. DEM is more computationally efficient than finite elements: In the present study, we ran more than 10,000 nonlinear DEM models with more than 5000 degrees of freedom each.

This study suggests two critical design elements to delay localization and maximize energy dissipation in staggered composites: (i) high control over the architecture to minimize statistical variations and (ii) interfaces with high $H\gamma_s^{(p)}/\tau_y$. These two strategies can be combined for best results, and interestingly both strategies are found in biological materials. Materials like collagen fibrils or nacre have a highly ordered, near-perfect periodic microstructure, and also make use of highly deformable interfaces (Barthelat et al., 2016) with hardening which may be generated by sacrificial bonds (Smith et al., 1999), nanofriction (Evans et al., 2001; Tai et al., 2006) or interface waviness (Barthelat et al., 2007). Duplicating these strategies in synthetic materials still presents formidable challenges to this day. Advanced fabrication methods such as self-assembly (Bonderer et al., 2008; Valashani et al., 2015), freeze casting (Deville et al., 2006), filtration (Liu et al., 2011), sedimentation (Behr et al., 2015), doctor blading (Mirkhalaf and Barthelat, 2016) or controlled mineralization (Mao et al., 2016) can be used to make staggered composites, but the morphological control these methods offer is still inferior to what is observed in biological materials. However, there are ways to fabricate perfectly periodic staggered arrangements at larger length scales in “architected materials”, using 3D printing (Espinosa et al., 2011) or laser engraving (Chintapalli et al., 2014; Valashani and Barthelat, 2015). Identifying synthetic materials for the interfaces also presents challenges. Various strategies were used to generate large deformations including metal or polymer ductility (Deville et al., 2006), polyelectrolytes (Tang et al., 2003), frictional contact (Barthelat and Zhu, 2011), or even polymer rheology (Chintapalli et al., 2014). When designing bio-inspired staggered composites, interfaces with large shear strain at failure and high hardening must be selected. These are indeed the two most important properties for the interfaces. Other properties such as stiffness, strength or even toughness are secondary for the interfaces and can these properties can be relatively low, provided that they are amplified by well-designed staggered architectures. As described in this article, we arrived at these conclusions using two-dimensional models of complex architectures which are, in reality, three dimensional. However, this simplification has enabled in the past unique insights into the mechanics of nacre-like materials, and we believe that the main conclusions reported here would be confirmed by three-dimensional models. Three-dimensional DEM models are more computationally expensive but more realistic, and could capture additional effects such as in-plane tablet rotations. These additional effects may have a non-negligible role on the overall response, but are beyond the scope of this article. The findings reported here can already be integrated to existing design guidelines (Begley et al., 2012; Barthelat, 2014; Gao, 2006) to further increase the performance of bio-inspired composites at the design stage.

Acknowledgments

This work was supported by a Strategic Grant (STPGP 479137 – 15) from the Natural Sciences and Engineering Research Council of Canada and by a Team Grant (191270) from the Fonds de Recherche du Québec – Nature et Technologies. N.A. was partially supported by a McGill Engineering Doctoral Award.

References

- Alava, M.J., Nukala, P.K., Zapperi, S., 2006. Statistical models of fracture. *Adv. Phys.* 55 (3–4), 349–476.
- Anup, S., 2015. Influence of initial flaws on the mechanical properties of nacre. *J. Mech. Behav. Biomed. Mater.* 46, 168–175.
- Askarinejad, S., Rahbar, N., 2015. Toughening mechanisms in bioinspired multilayered materials. *J. R. Soc. Interface* 12 (102).
- Bar-On, B., Wagner, H.D., 2011. Mechanical model for staggered bio-structure. *J. Mech. Phys. Solids* 59 (9), 1685–1701.
- Barthelat, F., Mirkhalaf, M., 2013. The quest for stiff, strong and tough hybrid materials: an exhaustive exploration. *J. R. Soc. Interface* 10 (89), 20130711.
- Barthelat, F., Rabiei, R., 2011. Toughness amplification in natural composites. *J. Mech. Phys. Solids* 59 (4), 829–840.
- Barthelat, F., Zhu, D., 2011. A novel biomimetic material duplicating the structure and mechanics of natural nacre. *J. Mater. Res.* 26 (10), 1203–1215.
- Barthelat, F., et al., 2007. On the mechanics of mother-of-pearl: a key feature in the material hierarchical structure. *J. Mech. Phys. Solids* 55 (2), 306–337.
- Barthelat, F., Yin, Z., Buehler, M.J., 2016. Structure and mechanics of interfaces in biological materials. *Nature Rev. Mater.* 1, 16007.
- Barthelat, F., 2014. Designing nacre-like materials for simultaneous stiffness, strength and toughness: optimum materials, composition, microstructure and size. *J. Mech. Phys. Solids* 73, 22–37.
- Begley, M.R., et al., 2012. Micromechanical models to guide the development of synthetic ‘brick and mortar’ composites. *J. Mech. Phys. Solids* 60 (8), 1545–1560.
- Behr, S., et al., 2015. Large-scale parallel alignment of platelet-shaped particles through gravitational sedimentation. *Sci. Rep.* 5.
- Bonderer, L.J., Studart, A.R., Gauckler, L.J., 2008. Bioinspired design and assembly of platelet reinforced polymer films. *Science* 319 (5866), 1069–1073.
- Chalkley, P., Chiu, W., 1993. An improved method for testing the shear stress/strain behaviour of adhesives. *Int. J. Adhes. Adhes.* 13 (4), 237–242.
- Chandler, M.Q., Cheng, J.-R.C., 2017. Discrete element modeling of microstructure of nacre. *Comput. Particle Mech.* 1–11.
- Chintapalli, R.K., et al., 2014. Strain rate hardening: a hidden but critical mechanism for biological composites? *Acta biomaterialia* 10 (12), 5064–5073.
- Dalaq, A.S., Ranganathan, S.I., Ostojia-Starzewski, M., 2013. Scaling function in conductivity of planar random checkerboards. *Sci.* 79, 252–261.
- Deville, S., et al., 2006. Freezing as a path to build complex composites. *Science* 311 (5760), 515–518.
- Dimas, L.S., Giesa, T., Buehler, M.J., 2014. Coupled continuum and discrete analysis of random heterogeneous materials: Elasticity and fracture. *J. Mech. Phys. Solids* 63, 481–490.
- Espinosa, H.D., et al., 2011. Tablet-level origin of toughening in abalone shells and translation to synthetic composite materials. *Nature Commun.* 2.
- Evans, A.G., et al., 2001. Model for the robust mechanical behavior of nacre. *J. Mater. Res.* 16 (9), 2475–2482.
- Gao, Y., Bower, A., 2004. A simple technique for avoiding convergence problems in finite element simulations of crack nucleation and growth on cohesive interfaces. *Model. Simul. Mater. Sci. Eng.* 12 (3), 453.
- Gao, H.J., 2006. Application of fracture mechanics concepts to hierarchical biomechanics of bone and bone-like materials. *Int. J. Fracture* 138 (1–4), 101–137.
- Ghaboussi, J., Barbosa, R., 1990. Three-dimensional discrete element method for granular materials. *Int. J. Numer. Analytical Methods Geomech.* 14 (7), 451–472.
- Gitman, I., Askes, H., Sluys, L., 2007. Representative volume: existence and size determination. *Eng. Fracture Mech.* 74 (16), 2518–2534.
- Guo, X., Gao, H., 2006. *Bio-inspired Material Design and Optimization*. Springer.
- Jäger, I., Fratzl, P., 2000. Mineralized collagen fibrils: A mechanical model with a staggered arrangement of mineral particles. *Biophys. J.* 79 (4), 1737–1746.
- Jackson, A.P., Vincent, J.F.V., Turner, R.M., 1988. The mechanical design of nacre. In: *Proceedings of the Royal Society of London. Series B, Biological Sciences*, 234, pp. 415–440.

- Kanit, T., et al., 2003. Determination of the size of the representative volume element for random composites: statistical and numerical approach. *Int. J. Solids Struct.* 40 (13), 3647–3679.
- Katti, D.R., Katti, K.S., 2001. Modeling microarchitecture and mechanical behavior of nacre using 3D finite element techniques. Part 1. Elastic properties. *J. Mater. Sci.* 36, 1411–1417.
- Keten, S., et al., 2010. Nanoconfinement controls stiffness, strength and mechanical toughness of [beta]-sheet crystals in silk. *Nat Mater* 9 (4), 359–367.
- Kotha, S.P., Li, Y., Guzelsu, N., 2001. Micromechanical model of nacre tested in tension. *J. Mater. Sci.* 36 (8), 2001–2007.
- Lim, R.K., et al., 2016. High-performance simulation of fracture in idealized 'brick and mortar' composites using adaptive Monte Carlo minimization on the GPU. *Int. J. High Perform. Comput. Appl.* 30 (2), 186–199.
- Liu, A.D., et al., 2011. Clay nanopaper with tough cellulose nanofiber matrix for fire retardancy and gas barrier functions. *Biomacromolecules* 12 (3), 633–641.
- Lu, Q., Bhattacharya, B., 2005. Analysis of randomness in mechanical properties of carbon nanotubes through atomistic simulation. 46th AIAA/ASME/ASCE/AHS/ASC Structures, Structural Dynamics and Materials Conference.
- Mao, L.B., et al., 2016. Synthetic nacre by pre-designed matrix-directed mineralization. *Science* 354 (6308), 107–110.
- Mathews, J.H., Fink, K.D., 2004. Numerical methods using MATLAB, 4. Pearson, London, UK.
- Mirkhalaf, M., Barthelat, F., 2016. Nacre-like materials using a simple doctor blading technique: Fabrication, testing and modeling. *J. Mech. Behav. Biomed. Mater.* 56, 23–33.
- Needleman, A., Tvergaard, V., 1991. A numerical study of void distribution effects on dynamic, ductile crack growth. *Eng. Fracture Mech.* 38 (2), 157–173.
- Nguyen, V.-D., et al., 2012. Imposing periodic boundary condition on arbitrary meshes by polynomial interpolation. *Comput. Mater. Sci.* 55, 390–406.
- Niebel, T.P., et al., 2016. Role of the polymer phase in the mechanics of nacre-like composites. *J. Mech. Phys. Solids* 96, 133–146.
- Ostoja-Starzewski, M., et al., 2007. On the size of representative volume element in elastic, plastic, thermoelastic and permeable random microstructures. In: Chandra, T., et al. (Eds.), *Thermec 2006*, Pts 1–5 201–+.
- Ostoja-Starzewski, M., 2006. Material spatial randomness: from statistical to representative volume element. *Probab. Eng. Mech.* 21 (2), 112–132.
- Press, W.H., et al., 1987. Numerical recipes: the art of scientific computing. AIP.
- Pro, J.W., et al., 2015. GPU-based simulations of fracture in idealized brick and mortar composites. *J. Mech. Phys. Solids* 80, 68–85.
- Pro, J.W., et al., 2015. The impact of stochastic microstructures on the macroscopic fracture properties of brick and mortar composites. *Extreme Mech. Lett.* 5, 1–9.
- Rabiei, R., Bekah, S., Barthelat, F., 2010. Failure mode transition in nacre and bone-like materials. *Acta Biomaterialia* 6 (10), 4081–4089.
- Ritchie, R.O., Buehler, M.J., Hansma, P., 2009. Plasticity and toughness in bone. *Phys. Today* 62 (6), 41–47.
- Smith, B.L., et al., 1999. Molecular mechanistic origin of the toughness of natural adhesives, fibres and composites. *Nature* 399 (6738), 761–763.
- Smith, B.L., et al., 1999. Molecular mechanistic origin of the toughness of natural adhesives, fibres and composites. *Nature (London)* 399 (6738), 761–763.
- Song, F., Soh, A.K., Bai, Y.L., 2003. Structural and mechanical properties of the organic matrix layers of nacre. *Biomaterials* 24 (20), 3623–3631.
- Song, F., Zhang, X.H., Bai, Y.L., 2011. Microstructure and characteristics in the organic matrix layers of nacre. *J. Mater. Res.* 17 (7), 1567–1570.
- Tai, K., Ulm, F.J., Ortiz, C., 2006. Nanogranular origins of the strength of bone. *Nano Lett.* 6 (11), 2520–2525.
- Tang, Z.Y., et al., 2003. Nanostructured artificial nacre. *Nature Mater.* 2 (6), 413 U8.
- Tsai, M.Y., Oplinger, D.W., Morton, J., 1998. Improved theoretical solutions for adhesive lap joints. *Int. J. Solids Struct.* 35 (12), 1163–1185.
- Valashani, S.M.M., Barthelat, F., 2015. A laser-engraved glass duplicating the structure, mechanics and performance of natural nacre. *Bioinspiration Biomimetics* 10 (2).
- Valashani, S.M.M., Barrett, C.J., Barthelat, F., 2015. Self-assembly of microscopic tablets within polymeric thin films: a possible pathway towards new hybrid materials. *RSC Adv.* 5 (7), 4780–4787.
- Volkersen, O., 1938. Die Nietkraftverteilung in zugbeanspruchten Nietverbindungen mit konstanten Laschenquerschnitten. *Luftfahrtforschung* 15 (1/2), 41–47.
- Wegst, U.G.K., Ashby, M.F., 2004. The mechanical efficiency of natural materials. *Philos. Mag.* 84 (21), 2167–2181.
- Wei, X., Filleter, T., Espinosa, H.D., 2015. Statistical shear lag model – Unraveling the size effect in hierarchical composites. *Acta Biomaterialia* 18, 206–212.
- Weiner, S., Addadi, L., 1997. Design strategies in mineralized biological materials. *J. Mater. Chem.* 7 (5), 689–702.
- Yin, X.L., et al., 2008. Statistical volume element method for predicting micro structure-constitutive property relations. *Comput. Methods Appl. Mech. Eng.* 197 (43–44), 3516–3529.
- Yourdkhani, M., Pasini, D., Barthelat, F., 2011. Multiscale mechanics and optimization of gastropod shells. *J. Bionic Eng.* 8 (4), 357–368.
- Zhang, Z.Q., et al., 2010. Mechanical properties of unidirectional nanocomposites with non-uniformly or randomly staggered platelet distribution. *J. Mech. Phys. Solids* 58 (10), 1646–1660.